PAPER

Hierarchical MoS$_2$ microspheres prepared through a zinc ion-assisted hydrothermal route as an electrochemical supercapacitor electrode†

Limei Xu,[a] Lin Ma, [ID] *[ab] Thitima Rujiralai,[c] Xiaoping Zhou,[a] Shanshan Wu[a] and Minling Liu[a]

Hierarchical molybdenum disulfide microspheres have been successfully prepared through a zinc ion-assisted hydrothermal route followed by an acid corrosion strategy. It is found that the MoS$_2$ microspheres comprised of numerous nanosheets with few-layered feature exhibit a 3D flower-like morphology. It is believed that the MoS$_2$/ZnS composites can act as a precursor for the formation of hierarchical MoS$_2$ microspheres. Additionally, the electrochemical properties of the as-prepared MoS$_2$ microspheres as an electrode material for supercapacitors have also been investigated. Compared with the MoS$_2$ nanosheet, the resultant MoS$_2$ microsphere demonstrates superior pseudcapacitive properties including high specific capacitance, good cycling and rate capability, which could be credited to its novel hierarchical architecture feature.

1. Introduction

The ever-increasing applications of portable electronic devices and electric vehicles have evoked intensive research interest for developing high-performance energy storage devices.[1] As a category of important energy storage devices, supercapacitors have received great attention for their many attractive merits such as excellent cycling stability, high specific capacitance and power density, good charging-discharging rates and safety.[2] According to the charge storage mechanism, supercapacitors can be divided into electric double-layer capacitors (EDLC) and pseudocapacitors (PC). Amongst them, pseudocapacitors can store charge by redox-based faradaic reactions, and thus can have higher capacitance values than EDLCs.[3] At present, one of key research themes of PCs is exploring new-type and high-performance electrode materials in order to achieve high capacity, long cycle life, high power/energy density and low cost.[4] A series of transition metal oxides such as RuO$_2$, CoO$_x$, NiO, MnO$_2$, and so forth, have been widely investigated as classic examples for pseudocapacitors.[5–8]

The discovery of graphene and its unusual properties have aroused interest in other layered materials.[9] Specially, layered transition-metal dichalcogenides which are characteristic of relatively weak interactions between the layers and the strong intralayer covalent bonding interactions have gained more and more attention due to their uncommon electronic, chemical and physical properties as well as potential applications in catalysis, sensors and energy generation and storage.[10–14] Thereinto, MoS$_2$ is a typical example existing in different forms such as 2H semiconductor phase (2H-MoS$_2$) and 1T metallic phase (1T-MoS$_2$) and has been reported to possess pseudocapacitive charge-storage property.[15–17] MoS$_2$ can store charge based on the ions intercalation into the layers of MoS$_2$ accompanied by a faradaic charge-transfer. This mechanism can be termed as intercalation pseudocapacitance.[18,19] Until now, a variety of MoS$_2$-based nanomaterials have been synthesized for supercapacitor applications.[20] For example, Huang hydrothermally synthesized 2H-MoS$_2$ nanosheets that demonstrated a specific capacitance of 129 F g^{-1} at 1 A g^{-1}.[21] However, inferior conductivity of 2H-MoS$_2$ would impair its electrochemical performance. To circumvent this issue, fabricating MoS$_2$ with metallic features and compositing MoS$_2$ with other conductive materials have been confirmed as effective ways. For instance, Chhowalla found that chemically exfoliated MoS$_2$ nanosheets contained a high concentration of the metallic 1T phase and can electrochemically intercalate H$^+$ and alkali metal ions with extraordinary efficiency.[22] Zhu *et al.* first employed hydrothermal techniques to synthesize water-coupled metallic MoS$_2$ nanosheets which exhibited excellent capacitive performances.[23] 2H-MoS$_2$/carbon nanotube and MoS$_2$/carbon aerogel hybrids were also prepared and delivered a high capacitance of 452 and 260 F g^{-1} at 1 A g^{-1}, respectively.[24,25] Additionally, the reduction of active surfaces originating from the overlapping or

[a]School of Chemistry and Chemical Engineering, Institute of Physical Chemistry, Development Center for New Materials Engineering & Technology in Universities of Guangdong, Lingnan Normal University, Zhanjiang 524048, P. R. China. E-mail: ma_lin75@126.com

[b]Department of Physics, Zhejiang University, Hangzhou 310027, P. R. China

[c]Department of Chemistry, Center of Excellence for Innovation in Chemistry, Faculty of Science, Prince of Songkla University, Songkhla, 90112, Thailand

† Electronic supplementary information (ESI) available. See DOI: 10.1039/c7ra05055k

restacking of MoS_2 nanosheets as well as structural instability during repeated ions insertion/extraction can also lead to an unsatisfied electrochemical performances.[26–28] Fabricating hierarchical MoS_2 nanostructures is considered to be an efficient pathway to solve this problem.[29,30] Hierarchical nanostructures, which are assembled from 0D, 1D and 2D nanomaterials as building blocks have attracted significant attention based on the fact that the hierarchical structures could supply efficient channels for transport of both electrons and ions, exhibit high surface area, shorten ion diffusion length, strengthen the structural stability and thus improve their electrochemical performance.[31–33] Various MoS_2 hierarchical nanostructures such as binder-free nanoarrays, nanosponges and nanoflowers have been reported to manifest superior electrochemical performances.[34–36]

In a liquid-phase synthetic route towards hierarchical MoS_2 nanostructures, some organics including surfactants, polymers, complexing agents, ionic liquids and amines were usually employed as a structure-directing agent which might produce pollutants leading to environmental damage.[37–40] Herein, we present a facile zinc ion-assisted hydrothermal method to prepare hierarchical MoS_2 microspheres assembled by 2D nanosheets, which exhibit superior electrochemical performance as an electrode for pseudcapacitor.

2. Experimental section

2.1 Zinc ion-assisted hydrothermal synthesis of hierarchical MoS_2 microspheres

In a typical synthesis, 1.5 mmol of zinc nitrate hexahydrate was dissolved in 30 mL deionized water to form a clear solution. Then 30 mL of 0.05 M sodium molybdate solution was slowly dropped into the above solution under vigorous stirring. No obvious precipitates can be observed. After that, 9 mmol of thiocarbamide was also dissolved into the above solution. Finally, the resulting solution was transferred into a 100 mL of Teflon-lined stainless steel autoclave and maintained at 240 °C for 24 h. Finally, the hydrothermal products were collected and redispersed into 0.5 M HCl solution to remove possible zinc sulfide residues. Then the products were washed with water and alcohol and dried at 60 °C for 6 h in a vacuum oven. The hydrothermal product was then annealed in a tube furnace at 500 °C for 2 h under nitrogen atmosphere to improve the crystallinity. For comparison, the MoS_2 nanosheets as well as ZnS products were also prepared by a similar method.

2.2 Characterizations

X-ray diffraction patterns (XRD) were obtained with a D/Max-2550 X-ray diffractometer using monochromatized CuKα radiation. TEM and HRTEM characterizations were carried out on a JEOL JFL-2010 TEM operating at 200 kV, for which the samples were prepared by dispersing them in acetone and drop-casting onto a 200 mesh copper grid coated with holey carbon. SEM observations were conducted by using a SIRION-100 field emission scanning electron microscopy (SEM). The elemental composition was analyzed by energy dispersive X-ray

spectroscopy (EDX, GENENIS-4000). X-ray photoelectron spectra (XPS) were processed on a Perkin-Elmer PHI5000c XPS, using C 1s (B. E. 284.6 eV) as a reference. Raman spectra were recorded using excitation with a 514 nm argon ion laser at 6 mW for 50 s on a Jobin Yvon LabRam HR spectrometer. The nitrogen sorption analysis was conducted at 77 K on a Quantachrome NOVA 2000e sorption analyzer and the Brunauer–Emmett–Teller (BET) surface area was estimated from the adsorption data. Electrochemical impedance spectroscopy (EIS) was obtained by applying a voltage amplitude of 5 mV in the frequency range from 100 kHz to 0.01 Hz on a CHI660E.

2.3 Electrochemical measurements

Electrochemical performance of the supercapacitor was studied by cyclic voltammetry (CV) and galvanostatic charge/discharge (GCD) at an electrochemical station (CHI660E). The electrochemical tests were performed in 3 M KOH electrolyte using a three electrode cell composed of a saturated calomel electrode (SCE) as reference, Pt plate as counter and the samples-based electrode as the working electrode. Working electrodes were fabricated by mixing electroactive material, carbon black and poly(vinylidene fluoride) in a mass ratio of 80 : 10 : 10 to obtain a slurry. Then the slurry was pressed onto the nickle foam current collector (1 cm^2) and dried at 60 °C for 12 h. The electroactive mass loading on the nickle foam is calculated to be 3.57 mg. The scan rate of the CV response varied from 5 to 100 mV s^{-1} with the potential range from −0.2 to 0.45 V. The capacitance values at various scan rate were calculated according to the CV curves as following eqn (1):

$$C = \int i \mathrm{d}V / 2v\Delta V \qquad (1)$$

The specific capacitances at different current density were calculated from the GCD curves according to eqn (2):

$$C = I\Delta t / \Delta Vm \qquad (2)$$

where C is the specific capacitance, $\int i \mathrm{d}V$ is the integrated area of the CV curves, v is the scan rate, ΔV is the potential window, I is the discharge current, Δt is the discharge time, m is the mass of the electroactive material loading on nickle foam.

3. Results and discussions

3.1 Microstructure and morphology of the samples

Fig. 1 shows the XRD patterns of the as-prepared MoS_2 nanosheets and MoS_2 microspheres. It is clearly seen that all the MoS_2 samples agree well with a hexagonal structure of MoS_2 (JCPDS 37-1492), in which the diffraction peaks at $2\theta = 14.2°$, $33.4°$, $39.8°$, $49.4°$, $59.1°$ and $69.8°$ can be unambiguously assigned to the (002), (100), (103), (105), (110) and (203) planes, respectively. No obvious peaks from the impurity ZnS phase can be observed in the XRD patterns of Fig. 1b, which confirms that residual zinc sulfide in hydrothermal products has been completely removed by the following acid treatment. The (002)
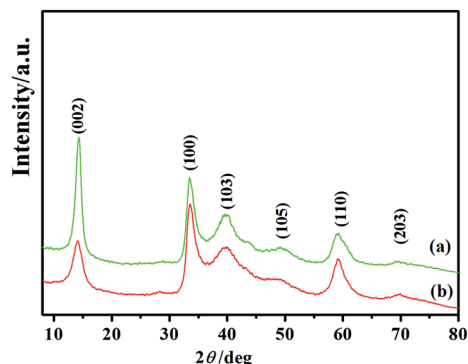
Fig. 1   XRD patterns of (a) the as-prepared MoS_2 nanosheets and (b) MoS_2 microspheres.

Fig. 2   SEM images of (a) MoS_2 nanosheets and (b) MoS_2 microspheres; (c) TEM image, (d) HRTEM image and (e) EDX pattern of MoS_2 microspheres.

reflection of layered MoS_2 at $2\theta = 14.2°$ can be indicative of an interlayer spacing of 0.62 nm according to Bragg's equation, which is in agreement with that of 2H phase MoS_2. In comparison with Fig. 1a, the prominently weakened (002) peak in Fig. 1b indicates that the crystal growth of MoS_2 layers were inhibited to a certain extent which might be due to the physical confinement of the ZnS produced in hydrothermal process. The stacking layers of MoS_2 microspheres could be estimated to be approximately ~5 layers in the light of FHWM of (002) reflection using Scherrer's equation, visibly less than those of the MoS_2 nanosheets (~11 layers).

Fig. 2a provides the morphology of the as-prepared MoS_2 nanosheets, which are scattered nanosheets. In sharp contrast to the MoS_2 nanosheets, Fig. 2b indicates that the MoS_2 products are hierarchical microspheres with sizes of ~1.5 μm. Moreover, it can be discerned that these MoS_2 microspheres are comprised of folded sheet-like subunits. The neighboring nanosheets on surface are interconnected and obvious open spaces exist between them. With a closer examination with TEM (Fig. 2c), these curled nanosheets stretch out towards the edges of the spheres and aggregate to form relatively loose microspheres. Fig. 2d clearly reveals the few-layered characteristic of the nanosheets in MoS_2 microspheres. These dispersed nanosheets display a 4–6 layer thickness with a lattice spacing of 0.62 nm between two adjacent layers, which is in line with XRD results. The de-layered structures can be favourable to decreasing the interlayer resistance and accelerating electron transfer between MoS_2 layers. The elemental composition of the MoS_2 microspheres were identified by EDX as shown in Fig. 2e. It can be seen that the MoS_2 spheres contain C, O, Mo and S elements. The little amount of C and O elements could come from the air adsorption. The atomic ratio of S to Mo is calculated as 2.07, which agrees with the MoS_2 stoichiometry.

The chemical states and compositions of the MoS_2 microspheres were studied by XPS. As shown in Fig. 3a, the Mo 3d orbit demonstrates two peaks located at 229.0 and 232.4 eV, which can be ascribed to the doublet of Mo(IV) $3d_{5/2}$ and Mo $3d_{3/2}$, respectively.[41,42] Besides, a small shoulder signal arising from 236.04 eV can be characteristic of a +6 oxidation state.[41,42] Fig. 3b reveals that the S 2p core-level XPS spectrum can be divided into two peaks, indicating existence of two chemical
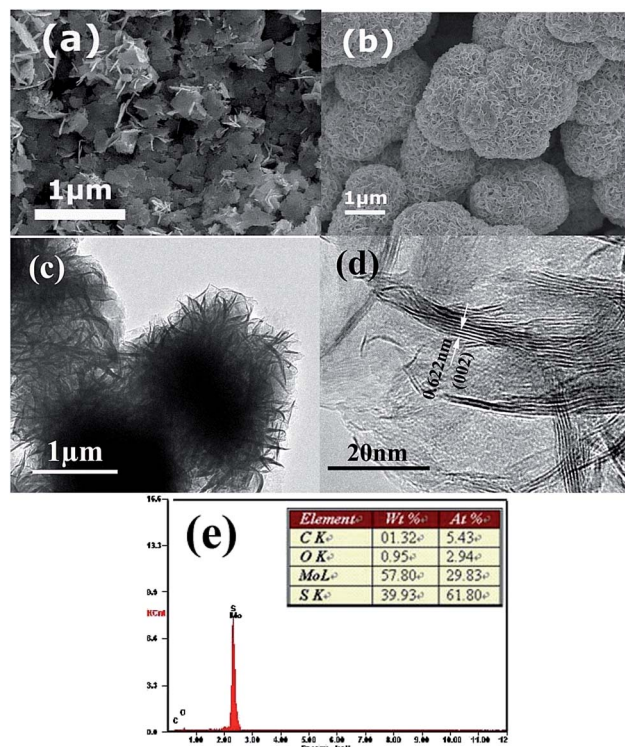
environments. The peaks at 161.95 and 163.09 eV can be attributed to the binding energies of S $2p_{3/2}$ and S $2p_{1/2}$.[41,42] The estimated atomic ratio of S : Mo is about 2.12, agreeing with the result of EDX.

Fig. 4 provides the Raman spectra of the as-prepared MoS_2 samples. The MoS_2 microspheres demonstrate two characteristic peaks situated at 378.25 cm^{-1} (E_{2g}^1 mode) and 402.24 cm^{-1} (A_{1g} mode). For the MoS_2 nanosheets, the peaks at 378.25 and 403.53 cm^{-1} correspond to E_{2g}^1 and A_{1g} mode. It is deemed that the E_{2g}^1 mode peak is related to the in-layer displacements of Mo and S atoms, whereas the A_{1g} mode peak involves the out-of-layer symmetric displacements of S atoms along the c-axis.[43,44] It is noticed that the intensities of E_{2g}^1 and A_{1g} peaks of the MoS_2 microspheres are lower than those of the MoS_2 nanosheets, suggesting some defect sites in the crystal structure of MoS_2.[45]

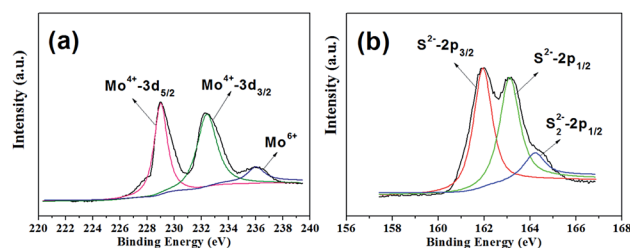Fig. 3   High-resolution XPS spectra of the as-prepared MoS_2 microspheres. (a) Mo 3d; (b) S 2p.
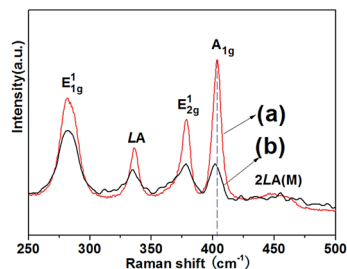
Fig. 4 Raman spectra of the as-prepared (a) MoS_2 nanosheets and (b) MoS_2 microspheres.

Besides, it can be discerned that the A_{1g} peak of MoS_2 microspheres has a down shift in comparison with that of the MoS_2 nanosheets, which further confirms the decreased layers.[46] In addition, the appearance of E_{1g}^1, LA as well as 2LA(M) peaks is associated with the vibration of one MoS_2 layer against neighboring layers and is called the rigid layer mode.[43,44]

The surface area of the as-prepared MoS_2 samples were determined by nitrogen adsorption–desorption isotherm measurements. A typical type IV can be observed in Fig. 5, indicating the presence of a mesoporous structure for both samples. The BET specific surface area of the MoS_2 microspheres was measured as about 28.39 m^2 g^{-1}, which is larger than that of the MoS_2 nanosheets (14.06 m^2 g^{-1}). The pore-size distribution plots of all samples were obtained from the adsorption branch of the N_2 adsorption–desorption isotherms by BJH method. It can be seen that the mesopores with a size of 3.4 nm are dominant in the MoS_2 nanosheets. By contrast, the presence of different pores (5.6 and 11.4 nm) for the MoS_2 microspheres can be observed with a broad pore-size distribution. Large surface area and porous feature are critical for affording more active sites for electrode reactions and promoting charge carriers transfer at the electrolyte/electrode interface, which results in observably enhanced electrochemical performances.

Time-dependent experiment was also carried out to investigate the formation process of the as-prepared MoS_2 hierarchical microspheres. It can been observed in Fig. 6a that spherical MoS_2/ZnS composites with numerous tiny nanoparticles on the surface were formed at the initial hydrothermal stage. Fig. 6b and c display that with the hydrothermal reaction proceeding,
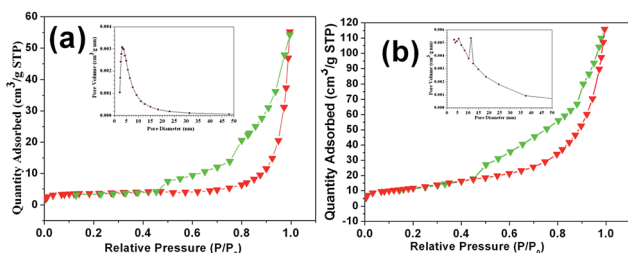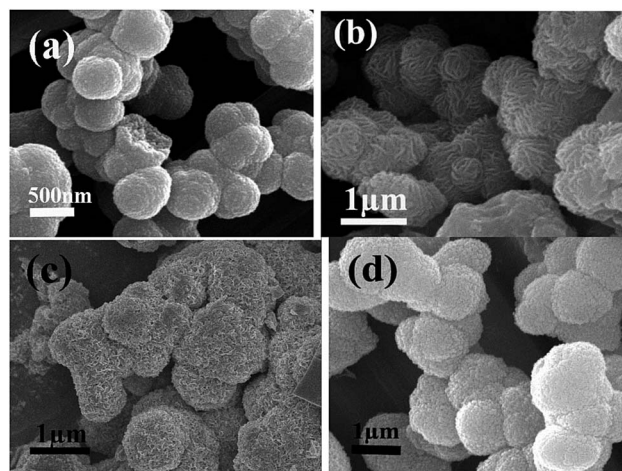

Fig. 6 SEM images of the MoS_2 samples prepared by zinc ion-assisted hydrothermal reaction at 240 °C for (a) 1 h, (b) 5 h, (c) 9 h, (d) SEM image of the ZnS samples prepared via a similar hydrothermal process at 240 °C for 24 h.

an increasing number of MoS_2 nanosheets appeared on the surfaces of the microspheres. For comparison, ZnS samples were also synthesized through a similar hydrothermal route as depicted in Fig. 6d, which manifested a sphere-like morphology.

Based on the above results, the formation of the hierarchical MoS_2 microspheres in our synthetic route can be illustrated in Fig. 7. Firstly, as MoO_4^{2-} anions were introduced to the Zn^{2+}-contained solution before hydrothermal treatment, no $ZnMoO_4$ precipitates appeared. The combination of Zn^{2+}–MoO_4^{2-} might be formed via strong electrostatic attraction. Secondly, during the following hydrothermal process, Zn^{2+} and MoO_4^{2-} ions reacted with H_2S arising from the decomposition of thiocarbamide to produce small ZnS and MoS_2 nanoparticles, respectively. Due to the high surface energy, these nanoparticles were liable to aggregate together to form spherical composite particles. Owing to the anisotropic characteristic, the MoS_2 nanoparticles began to evolve into 2D nanosheets. These nanosheets gradually grew larger, interconnected together to form MoS_2 nanosheets/ZnS microspheres. With removal of ZnS by acid erosion, the MoS_2 microspheres could be obtained. The detailed formation mechanism needs to be further investigated.

3.2 Electrochemical performance of the sample electrodes

The pseudocapacitive properties of the MoS_2 sample electrodes was tested in a 3 M KOH aqueous electrolyte. The CV curves of
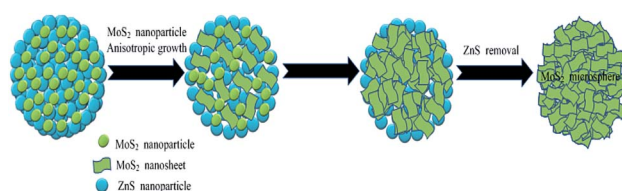

Fig. 5 Nitrogen adsorption–desorption isotherm of (a) MoS_2 nanosheets and (b) MoS_2 microspheres. The inserted figure is the pore-size distribution.

Fig. 7 Illustration of the formation process of the MoS_2 microspheres.

both MoS_2 electrodes were plotted in Fig. 8a for comparison. Evidently, the CV curves of two electrodes are different from the ideal rectangular curves originating from the electric double-layer capacitance, indicating a typical pseudocapacitive mechanism according to the redox peaks.[2,3] The prominent cathodic peaks situated at around 0.16–0.20 V can be attributed to the electrochemical insertion of K^+ ions into the MoS_2 interlayer. The corresponding anodic peaks located at about 0.27–0.32 V can be attributed to the extraction of K^+ ions from layered MoS_2.[15–19] The nearly symmetrical redox peaks are indicative of high reversibility of the insertion/extration process. As is well known, the specific capacitance is proportional to the area of the CV curves.[2,3] It is apparent that the MoS_2 microspheres possess a much larger CV curve area than that of MoS_2 nanosheets, demonstrating that the MoS_2 microspheres have a higher capacitance value. Moreover, it can be seen that the CV area of pure Ni foam is almost negligible compared with those of the MoS_2 electrodes, revealing the almost no capacitance contribution of the current collector. The CV curves under the different sweep rates are displayed in Fig. 8b and c, respectively. As the scan rate increases, CV curves of all the electrodes still retain a similar shape in spite of a small shift of peak positions owing to the polarization effect.[47] The area under the curve increased with increasing scan rate, meaning that the MoS_2 electrodes show the ideal supercapacitive behavior. The increase in current with increasing scan rate indicates that the kinetics of the interfacial faradic redox reactions and the rates of electronic and ionic transmission are rapid enough at scan rates as high as 100 mV s^{-1}.[48] Fig. 8d shows the change in scan rate with respect to the specific capacitance. With the scan rate increasing from 5 mV s^{-1} to 100 mV s^{-1}, according to eqn (1), the specific capacitances of MoS_2 nanosheet and MoS_2 microsphere electrodes decrease from 211.3 to 85.1 F g^{-1} and 294.4 to

209.2 F g^{-1}, respectively. Obviously, MoS_2 microsphere electrode delivers a higher capacitance retention of 71% than that of MoS_2 nanosheet electrode (40%). The decrease in capacitance could be attributed to the presence of inner active sites, which cannot sustain the redox transitions completely at higher scan rates.[48]

Galvanostatic charge–discharge was carried out to measure the specific capacitance of electrochemical capacitors at constant current. Fig. 9a shows galvanostatic charge–discharge curves of the MoS_2 nanosheet and MoS_2 microsphere electrodes at a current density of 1 A g^{-1}, respectively. Apparently, the latter manifests a longer discharging time than that of the former, representing a higher discharge capacitance, which is in agreement with CV results. Fig. 9b and c show charge–discharge curves of the two electrodes at various current densities. For the MoS_2 nanosheet electrode, according to eqn (2), the discharge specific capacitance values are calculated to be 217.3, 143.4, 124.3, 90.6 and 58.1 F g^{-1} at 0.5, 1, 2, 4 and 10 A g^{-1}, respectively. By contrast, the MoS_2 microsphere electrode delivers a much higher capacitance of 294.6, 254.0, 185.7, 157.8 and 134.1 F g^{-1} at 0.5, 1, 2, 4 and 10 A g^{-1}, respectively. The relationship between specific capacitance and current density is illustrated in Fig. 9d. MoS_2 microsphere exhibits a capacitance of 134.1 F g^{-1} at 10 A g^{-1} with a capacitance retention of 46% relative to 0.5 A g^{-1}. In contrast, the MoS_2 nanosheet electrode delivers a much smaller capacitance value of 58.1 F g^{-1} at 10 A g^{-1} with only 27% retention compared with 0.5 A g^{-1}. The greatly enhanced electrochemical performances of MoS_2 microsphere can be attributed to the robust 3D hierarchical architecture, which can be favorable to offering sufficient surface area for electrochemical reactions and promoting charge carriers transfer at the electrolyte/electrode interface.

Furthermore, the good electrochemical properties of the MoS_2 microsphere electrode were further confirmed by the
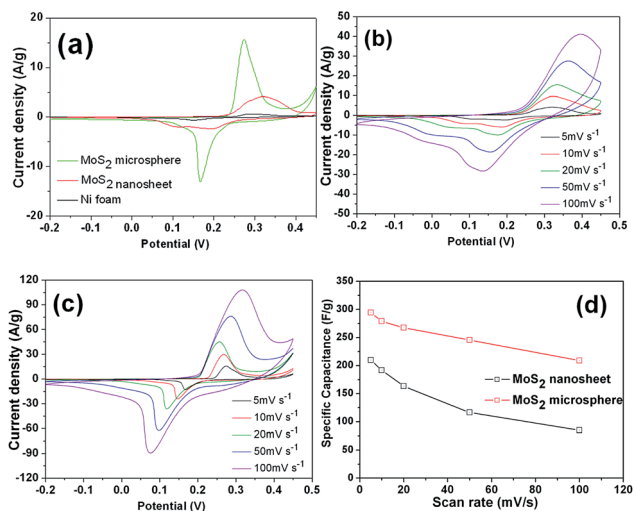

Fig. 8 Electrochemical measurements of MoS_2 nanosheet and MoS_2 microsphere electrodes: (a) cyclic voltammograms (CV) within the optimized potential range of −0.2 to 0.45 V in 3 M KOH solution at a scan rate of 5 mV s^{-1}, voltammetric responses of (b) MoS_2 nanosheet and (c) MoS_2 microsphere electrodes at various scan rates, (d) specific capacitance obtained at different scan rates.
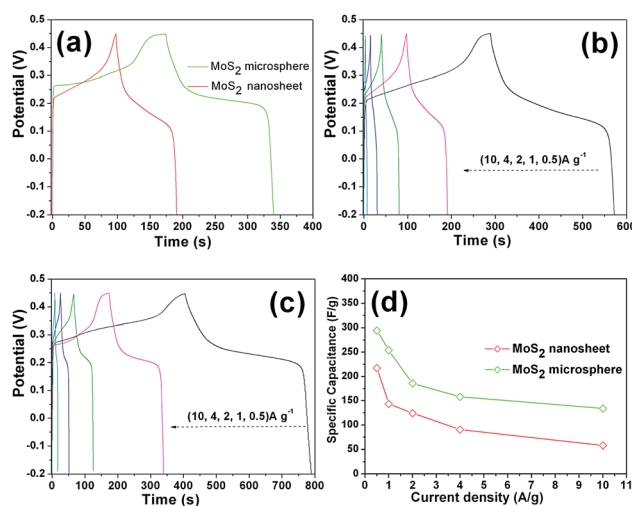

Fig. 9 (a) Galvanostatic charge–discharge curves of the MoS_2 sample electrodes at 1 A g^{-1}; galvanostatic charge–discharge curves of (b) the MoS_2 nanosheet electrode and (c) the MoS_2 microsphere electrode at different current densities; (d) specific discharge capacitances *vs.* current densities of the two sample electrodes.
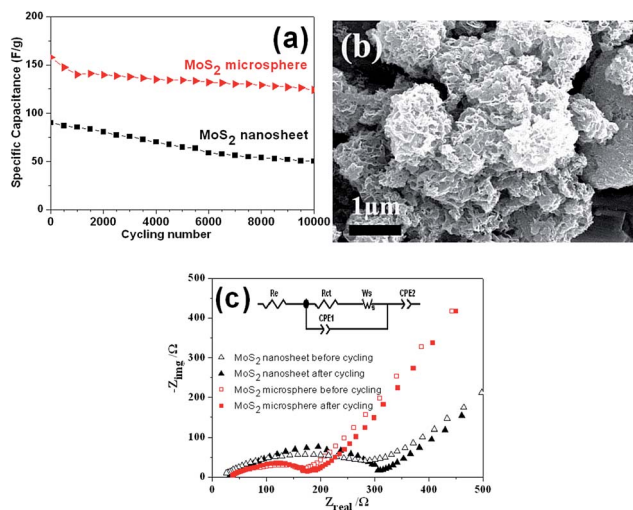
Fig. 10 (a) Cycling performance of the as-prepared MoS_2 sample electrodes at 4 A g^{-1}, (b) SEM image of the MoS_2 microspheres after cycling and (c) EIS spectra of the sample electrodes before and after cycling, inset is the equivalent circuit.

long-term cycling test. As shown in Fig. 10a, during 10 000 cycles testing, the MoS_2 nanosheet electrode exhibits an obvious capacitance loss up to 44.3%. The obvious decay in capacitance may be caused by chemical dissolution and ion intercalation/deintercalation induced volume change of active materials. For MoS_2 microsphere electrode, still 78.5% of the initial capacitance can be maintained after long-term cycles. The capacitive decay observed for MoS_2 microsphere electrode during the process of the charge–discharge cycling can be attributed to the partial collapse of the MoS_2 microsphere as shown in Fig. 10b. In comparison with MoS_2 nanosheets, the prominently enhanced electrochemical performances of MoS_2 microspheres can be attributed to the 3D hierarchical architecture, which can be favorable to maintaining structural integrity, offering sufficient surface area for electrochemical reactions and promoting charge carriers transfer at the electrolyte/electrode interface.

EIS measurements were performed to understand why MoS_2 microsphere electrode exhibits a superior electrochemical performance. Fig. 10c displays that both impedance spectra are composed of semicircles in the high frequency region followed by a linear slope in the low frequency region. The diameter of the characteristic depressed semicircle in the high frequency regions is related to charge transfer resistance. A linear region in the low-frequency range corresponds to the diffusive resistance (Warburg impedance). The steeper straight line of MoS_2 microsphere reveals a faster ion diffusion in comparison with MoS_2 nanosheet. The equivalent circuit (inset of Fig. 10c) for fitting the EIS data contains the internal resistance (R_e), the charge transfer resistance (R_{ct}), the constant phase element (CPE_1, CPE_2) involving the double layer capacitance and the limit capacitance, and Warburg impedance (W_s).[21,49] The R_e represents a combined resistance of ionic resistance of electrolyte, intrinsic resistance of substrate, and contact resistance at the active material/current collector interface. The R_{ct} is

Table 1 R_{ct} values of the MoS_2 nanosheet and MoS_2 microsphere electrodes before and after cycling

Sample electrode	R_{ct}/Ω	
	Before cycling	After cycling
MoS_2 nanosheet	282.3	298.4
MoS_2 microsphere	139.8	147.5

caused by faradaic redox process. The W_s is a result of the frequency dependence of ion diffusion/transport in the electrolyte to the electrode surface. The smaller diameter of the Nyquist circle of MoS_2 microsphere means a fast electron transfer process at the electrode/electrolyte interface.[50] In addition, it is noted that the diameter of the Nyquist circle after cycling became slightly larger, indicating an increasement of R_{ct}, which is probably due to the loss of adhesion of some active material with the current collector during the charge/discharge cycling.[49,51] The R_{ct} values obtained by data fitting according to the equivalent circuit model are summarized in Table 1.

4. Conclusions

In conclusion, hierarchical MoS_2 microspheres composed of few-layered nanosheets have been successfully synthesized *via* a facile zinc ion-assisted hydrothermal route combined with an acid erosion method. It is found that the initially generated MoS_2/ZnS composites acted as a precursor for the formation of the hierarchical MoS_2 microspheres. Furthermore, the hierarchical MoS_2 microspheres deliver a high specific capacitance as well as good rate and cycle ability for supercapacitor.

Acknowledgements

Notes and references

1 R. Sahoo, A. Pal and T. Pal, *Chem. Commun.*, 2016, **52**, 13528–13542.
2 Y. Zheng, Y. Yang, S. Chen and Q. Yuan, *CrystEngComm*, 2016, **18**, 4218–4235.
3 Y. Wang, Y. Song and Y. Xia, *Chem. Soc. Rev.*, 2016, **45**, 5925–5950.
4 G. Wang, L. Zhang and J. Zhang, *Chem. Soc. Rev.*, 2012, **41**, 797–828.
5 B. Shen, X. Zhang, R. Guo, J. Lang, J. Chen and X. Yan, *J. Mater. Chem. A*, 2016, **4**, 8180–8189.

6 X. Y. Liu, Y. Q. Gao and G. W. Yang, *Nanoscale*, 2016, **8**, 4227–4235.

7 J. Min, J. Liu, M. Lei, W. Wang, Y. Lu, L. Yang, Q. Yang, G. Liu and N. Su, *ACS Appl. Mater. Interfaces*, 2016, **8**, 780–791.

8 T. Zhai, X. Lu, F. Wang, H. Xia and Y. Tong, *Nanoscale Horiz.*, 2016, **1**, 109–124.

9 C. N. R. Rao, H. S. S. R. Matte and U. Maitra, *Angew. Chem., Int. Ed.*, 2013, **52**, 13162–13185.

10 J. Yang and H. S. Shin, *J. Mater. Chem. A*, 2014, **2**, 5979–5985.

11 K. J. Huang, Y. J. Liu, H. B. Wang, Y. Y. Wang and Y. M. Liu, *Biosens. Bioelectron.*, 2014, **55**, 195–202.

12 L. X. Fang, K. J. Huang and Y. Liu, *Biosens. Bioelectron.*, 2015, **71**, 171–178.

13 K. J. Huang, Y. J. Liu, Y. M. Liu and L. L. Wang, *J. Hazard. Mater.*, 2014, **276**, 207–215.

14 D. Chen, W. Chen, L. Ma, G. Ji, K. Chang and J. Y. Lee, *Mater. Today*, 2014, **17**, 184–193.

15 B. Wang, Q. Wu, H. Sun, J. Zhang, J. Ren, Y. Luo, M. Wang and H. Peng, *J. Mater. Chem. A*, 2017, **5**, 925–930.

16 K. Krishnamoorthy, P. Pazhamalai, G. K. Veerasubramani and S. J. Kim, *J. Power Sources*, 2016, **321**, 112–119.

17 G. Zhang, H. Liu, J. Qu and J. Li, *Energy Environ. Sci.*, 2016, **9**, 1190–1209.

18 S. K. Balasingam, J. S. Lee and Y. Jun, *Dalton Trans.*, 2015, **44**, 15491–15498.

19 B. Xie, Y. Chen, M. Yu, T. Sun, L. Lu, T. Xie, Y. Zhang and Y. Wu, *Carbon*, 2016, **99**, 35–42.

20 G. Zhang, H. Liu, J. Qu and J. Li, *Energy Environ. Sci.*, 2016, **9**, 1190–1209.

21 K. J. Huang, J. Z. Zhang, G. W. Shi and Y. M. Liu, *Electrochim. Acta*, 2014, **132**, 397–403.

22 M. Acerce, D. Voiry and M. Chhowalla, *Nat. Nanotechnol.*, 2015, **10**, 313–318.

23 X. Geng, Y. Zhang, Y. Han, J. Li, L. Yang, M. Benamara, L. Chen and H. Zhu, *Nano Lett.*, 2017, **17**, 1825–1832.

24 K. J. Huang, L. Wang, J. Z. Zhang, L. L. Wang and Y. P. Mo, *Energy*, 2014, **67**, 234–240.

25 K. J. Huang, L. Wang, J. Z. Zhang and K. Xing, *J. Electroanal. Chem.*, 2015, **752**, 33–40.

26 H. Ji, C. Liu, T. Wang, J. Chen, Z. Mao, J. Zhao, W. Hou and G. Yang, *Small*, 2015, **11**, 6480–6490.

27 R. Kumuthini, R. Ramachandran, H. A. Therese and F. Wang, *J. Alloys Compd.*, 2017, **705**, 624–630.

28 L. Wang, Y. Ma, M. Yang and Y. Qi, *Appl. Surf. Sci.*, 2017, **396**, 1466–1471.

29 R. Zhou, C. J. Han and X. M. Wang, *J. Power Sources*, 2017, **352**, 99–110.

30 S. Zhang, R. Hu, P. Dai, X. Yu, Z. Ding, M. Wu, G. Li, Y. Ma and C. Tu, *Appl. Surf. Sci.*, 2017, **396**, 994–999.

31 L. Wang, Y. Ma, M. Yang and Y. Qi, *Electrochim. Acta*, 2015, **186**, 391–396.

32 Y. Ma, Y. Jia, L. Wang, M. Yang, Y. Bi and Y. Qi, *J. Power Sources*, 2017, **342**, 921–928.

33 Y. Wang, L. Yu and X. W. Lou, *Angew. Chem., Int. Ed.*, 2016, **55**, 7423–7426.

34 K. Krishnamoorthy, G. K. Veerasubramani, P. Pazhamalai and S. J. Kim, *Electrochim. Acta*, 2016, **190**, 305–312.

35 S. K. Balasingam, M. Lee, B. H. Kim, J. S. Lee and Y. Jun, *Dalton Trans.*, 2017, **46**, 2122–2128.

36 X. Wang, J. Ding, S. Yao, X. Wu, Q. Feng, Z. Wang and B. Geng, *J. Mater. Chem. A*, 2014, **2**, 15958–15963.

37 P. Sun, W. Zhang, X. Hu, L. Yuan and Y. Huang, *J. Mater. Chem. A*, 2014, **2**, 3498–3504.

38 H. Y. Wang, B. Y. Wang, D. Wang, L. Lu, J. G. Wang and Q. C. Jiang, *RSC Adv.*, 2015, **5**, 58084–58090.

39 J. Li, D. Wang, H. Ma, Z. Pan, Y. Jiang, M. Li and Z. Tian, *Mater. Lett.*, 2015, **160**, 550–554.

40 L. Ma, L. M. Xu, X. P. Zhou and X. Y. Xu, *Mater. Lett.*, 2014, **132**, 291–294.

41 Y. Yan, B. Xia, N. Li, Z. Xu, A. Fisher and X. Wang, *J. Mater. Chem. A*, 2015, **3**, 131–135.

42 J. Zhou, J. Qin, X. Zhang, C. Shi, E. Liu, J. Li, N. Zhao and C. He, *ACS Nano*, 2015, **9**, 3837–3848.

43 K. G. Zhou, F. Withers, Y. Cao, S. Hu, G. Yu and C. Casiraghi, *ACS Nano*, 2014, **8**, 9914–9924.

44 S. Y. Chen, C. Zheng, M. S. Fuhrer and J. Yan, *Nano Lett.*, 2015, **15**, 2526–2532.

45 L. Zhang, W. Fan and T. Liu, *RSC Adv.*, 2015, **5**, 43130–43140.

46 H. Li, Q. Zhang, C. C. R. Yap, B. K. Tay, T. H. T. Edwin, A. Olivier and D. Baillargeat, *Adv. Funct. Mater.*, 2012, **22**, 1385–1390.

47 H. Wang, H. Yi, X. Chen and X. Wang, *J. Mater. Chem. A*, 2014, **2**, 1165–1173.

48 J. Zhang, H. Feng, Q. Qin, G. Zhang, Y. Cui, Z. Chai and W. Zheng, *J. Mater. Chem. A*, 2016, **4**, 6357–6367.

49 Z. Fan, J. Yan, T. Wei, L. Zhi, G. Ning, T. Li and F. Wei, *Adv. Funct. Mater.*, 2011, **21**, 2366–2375.

50 S. E. Moosavifard, M. F. El-Kady, M. S. Rahmanifar, R. B. Kaner and M. F. Mousavi, *ACS Appl. Mater. Interfaces*, 2015, **7**, 4851–4860.

51 A. Ramadoss, T. Kim, G. S. Kim and S. J. Kim, *New J. Chem.*, 2014, **38**, 2379–2385.